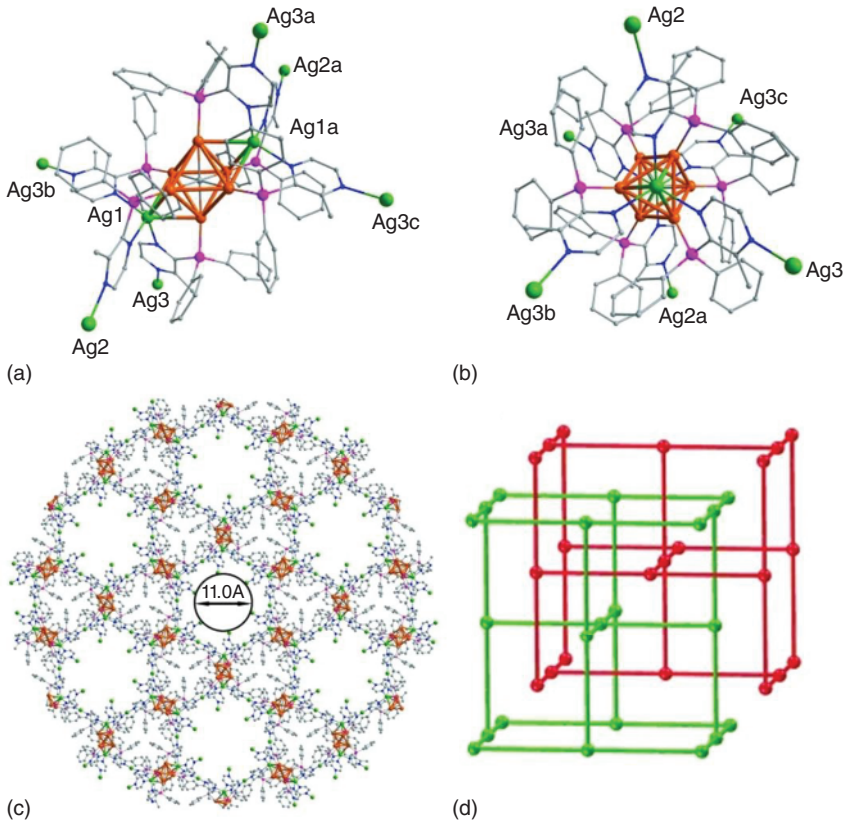

Figure 1.11 (a, b) Crystal structure of the C-$Au_6Ag_6(mdppz)_6$ nano-building block in different views. (c) Perspective view of Au_6Ag_6 cluster-based MOFs along the [0 0 1] direction. (d) Schematic illustration of the NbO topology in the twofold interpenetrated Au_6Ag_6 cluster-based MOFs. Colors: orange sphere, Au; green sphere, Ag; purple sphere, P; gray sphere, C; blue sphere, N. Source: Reproduced with permission from Ref. [52]. © 2014 John Wiley & Sons.

$Au_4(MHA)_4$ cluster was synthesized in an aqueous medium by adding excess mercaptohexanoate (MHA, S-$(CH_2)_5COO^-$) ligand to $HAuCl_4{\cdot}3H_2O$ solution. Then, Zn^{2+} ion is introduced to induce the assembly between monomeric $Au_4(MHA)_4$ clusters without changing the original structure of the gold cluster. The mercaptohexanoic acid (MHA–H) acts as a protecting ligand as well as a mild reductant that reduces Au(III) to Au(I). The formation of GCA is induced by introducing metal ions into the solution of $Au_4(MHA)_4$ cluster because metal ions can guide the formation of the superstructure from monomeric building blocks. The $Au_4(MHA)_4$ clusters are successfully assembled by the interaction between the anionic carboxylate group in the MHA ligand and Zn^{2+} ion in a cross-linking fashion.

The authors showed that unique aurophilic interaction between Au_4 clusters is responsible for the radiative channel that is unprecedented for conventional gold NCs and nanoparticles. And the rigidified chemical environment, which was

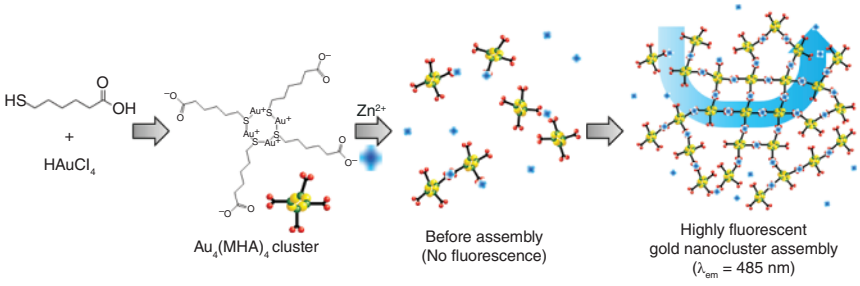

Figure 1.12 Synthesis of GCA. Source: With permission from Ref. [53]. © 2021 American Chemistry Society.

induced by the coordination of Zn^{2+} ion with the carboxylate group in the ligand, to delay vibrational relaxation accounts for the bright greenish-blue fluorescence.

Recently, the Yam group constructed an unprecedented gold(I) cluster cage $[Au_{24}\text{-}Cl]_C$ with $[(\mu_3\text{-}S)Au_3]^+$ units as the nodes or vertices and V-shaped 1,3-bis (diphenylphosphino)benzene ligand with 2-phenyl substituent as the organic building block [54]. The complex cation of $[Au_{24}\text{-}Cl]_C$ displays a cubic structure, where eight $[(\mu_3\text{-}S)Au_3]^+$ units occupy the vertices with the 12 diphosphine ligands spanning the edges of the cube. By virtue of the dynamic and reversible nature of the coordination bonds and aurophilic interactions, the gold(I) cluster cages exhibit interesting stimuli-responsive properties. A change of the counterions from Cl^- to PF_6^- or BF_4^- resulted in a structural transformation from a cubic structure of $[Au_{24}\text{-}PF_6]_C$ and $[Au_{24}\text{-}BF_4]_C$ to a rhombic prism structure of $[Au_{24}\text{-}PF_6]_{RP}$ and $[Au_{24}\text{-}BF_4]_{RP}$ during the crystallization process, which could be recovered upon dissolution. The complex cations of $[Au_{24}\text{-}PF_6]_{RP}$ and $[Au_{24}\text{-}BF_4]_{RP}$ display rhombic prism structures with two rhomboidal and four square faces, and the bidentate phosphine ligands occupy the 12 edges and are linked by eight $[(\mu_3\text{-}S)Au_3]^+$ vertices. Furthermore, upon heating the CD_3CN solution of $[Au_{24}\text{-}PF_6]_C$ at 353 K for around 0.5 hour, $[Au_{18}\text{-}PF_6]_{TP}$ was afforded, which displayed a triangular prism structure with six $[(\mu_3\text{-}S)Au_3]^+$ units occupying the vertices and nine ligands spanning the edges (Figure 1.13). The reverse transformation from $[Au_{18}\text{-}PF_6]_{TP}$ to $[Au_{24}\text{-}PF_6]_C$ could be realized in DMSO-d_6, CD_3CN, and acetone-d_6 solutions at room temperature. This work suggests a new perspective to construct GCAMs by predesigning the ligands and cluster nodes with the desired geometry and configuration.

1.4 Applications

Directional modification and functionalization of gold NCs through surface engineering could expand the potential applications of this kind of materials. On the other hand, besides the inherent properties of the individual metal clusters, the aggregation form of the gold NCs in GCAMs usually facilitates novel light, electricity, and magnetic behaviors that benefit from the unobstructed intercluster electronic communication.

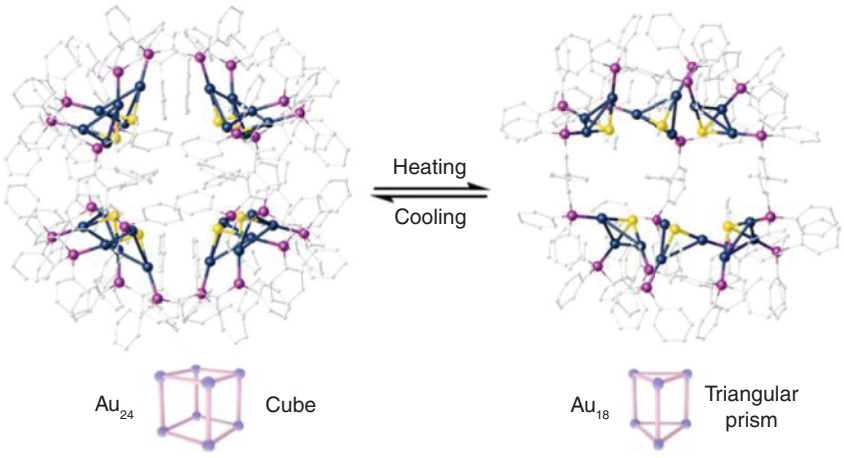

Figure 1.13 The structure transformation between the cubic Au_{24} cage and the triangular prism Au_{18} cage. Source: With permission from Ref. [54]. © 2021 American Chemical Society.

1.4.1 Biomedical Application

The GCA based on Au_4 clusters and Zn^{2+} can be disassembled and reassembled by the extraction and readdition of metal ions with the original structure of the Au_4 cluster maintained during the disassembly process [53]. Both the controllability of the dis/reassembly process and their structural similarity to metal–organic frameworks enable GCA to be applied as a biodegradable drug delivery system (DDS) that can be monitored by the distinct PL during its degradation and drug release. The representative anticancer drug, doxorubicin, was loaded into GCA to demonstrate its potential use as a trackable drug delivery vehicle. The hydrophobic doxorubicin can be successfully loaded inside GCA without changing the characteristic emission wavelength of GCA (Figure 1.14a). Gradual disassembly and drug release of drug-loaded GCA were confirmed by the decrease of PL and the increase of released drug in the solution (Figure 1.14a,b). Interestingly, the rate of drug release can be controlled by the rate of disassembly. The release rate of doxorubicin increases after 20 hours from the addition of the EDTA solution to the drug-loaded GCA. Cell viability analysis also confirms both the biocompatibility of GCA and its capability as a drug delivery vehicle, presenting efficient drug loading and release and sustaining the anticancer effect of doxorubicin (Figure 1.14c). Finally, cell imaging by confocal fluorescence microscopy was conducted to evaluate the performance of doxorubicin-loaded GCA as the trackable and self-indicating DDS (Figure 1.14d,e). Time-dependent confocal microscopy shows the gradual release of doxorubicin in the HeLa cell (Figure 1.14d,e, red) simultaneously with the dimming fluorescence of GCA (Figure 1.14d,e, blue). These unique features of strong fluorescence, with narrow wavelength following the degradation/disassembly status of the vehicle and release of the drug cargo, confirm the great potential of GCA as a trackable and degradable material, expanding theragnostic drug delivery in the future.

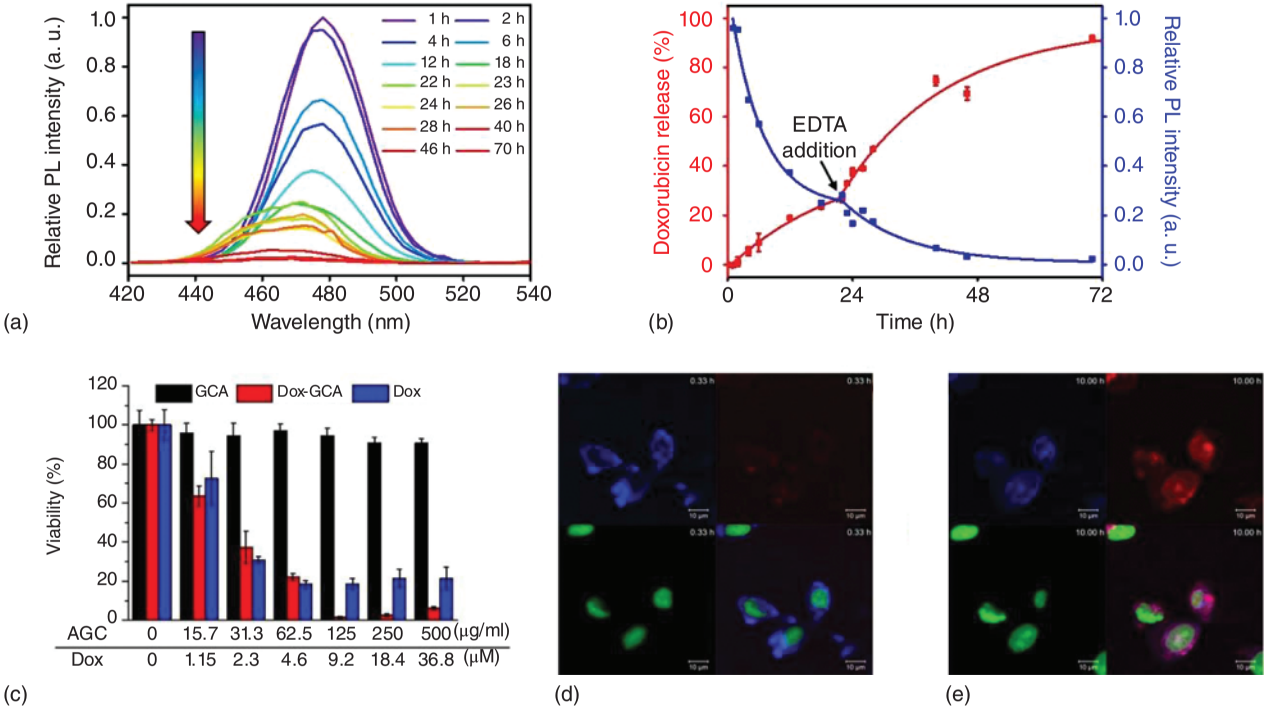

Figure 1.14 (a) Time-dependent change of PL spectrum of doxorubicin-loaded GCAs. (b) Release profiles of doxorubicin from Dox-GCA, and the PL intensity of GCA during release. EDTA was added at 22 hours to boost the release rate. (c) Evaluation of biocompatibility of GCA and anticancer effect of Dox-GCAs compared with free doxorubicin. (d, e) Confocal microscopy images of HeLa cells after the treatment of drug-loaded GCAs. 20 minutes after (d) and 10 hours after the treatment. Each color notes the emission from GCAs (blue), doxorubicin (red), and Draq5 (green, nucleus-staining). Source: Reproduced with permission from Ref. [53]. © 2021 American Chemistry Society.

1.4.2 Semiconductivity

$(AuAg)_{34n}$ comprises polymeric chains parallel to the *c*-axis of the single crystal, and these chains with direct metal–metal bonds connecting the clusters are separated in *a*- and *b*-directions by the bulky A-Adm ligands. This structural anisotropy promises a highly anisotropic (semi)conductivity. To prove this, FET devices were fabricated to measure the direction-dependent conductivity of the polymer crystals (Figure 1.15a). All the field-effect transistors showed an anisotropy of electrical conductivity (Figure 1.15b). The averaged electrical conductivity along the *c*-crystallographic axis of the crystal at room temperature and relative humidity of 56% is $1.49 \times 10^{-5}\,S\,m^{-1}$, which is 1800 times the electrical conductivity along the *a*-crystallographic axis.

The semiconductor properties of a single crystal along the *c*-crystallographic axis were studied with the transfer and output characteristic curves (Figure 1.15c,d).

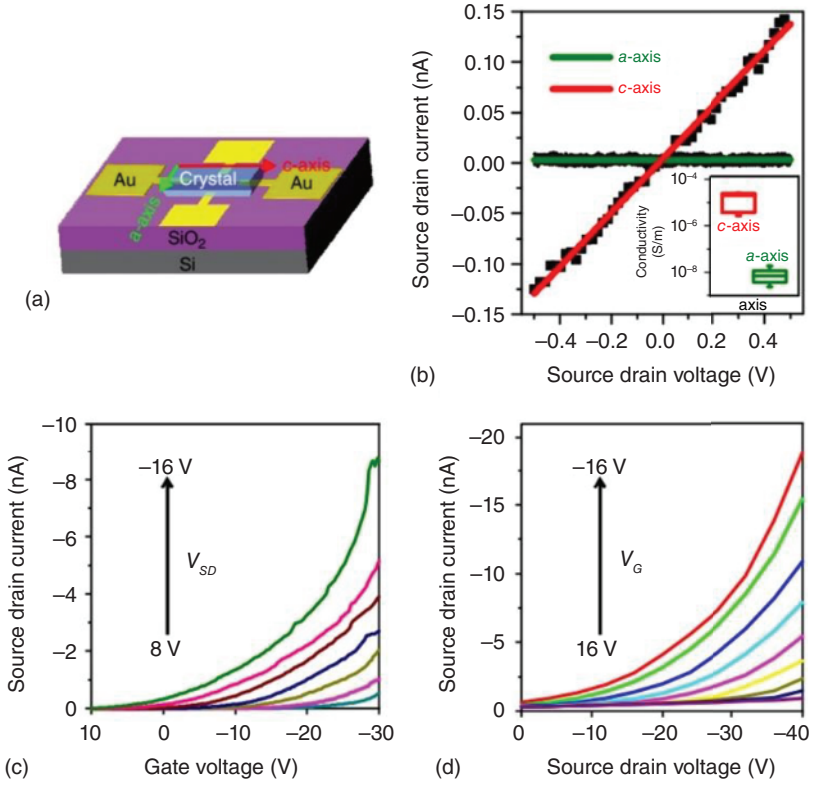

Figure 1.15 Electrical transport properties of the cluster polymer crystals. (a) The structure of the polymer crystal FET. (b) I–V plot of the polymer crystal along the *a*-axis and *c*-axis, respectively, with the range of corresponding conductivity values shown in the inset. (c) Transistor transfer (VSD = 8 to −16 V in −4 V steps), and (d) output characteristics (VG = 16 to −16 V in −4 V steps) measured along the *c*-axis of the polymer crystal. Channel length, width = 80, 50 μm. Source: With permission from Ref. [47]. © 2019 Springer Nature Limited.

The transfer curves show that at negative gate voltage (V_G), the source-drain currents increase with more negative V_G, demonstrating the p-type field effect. This indicates a hole conduction mechanism. The ON/OFF current ratio is around 4000, and the charge carrier mobility reaches 2.46×10^{-2} cm^2 V^{-1} s^{-1} at source-drain voltage (V_{SD}) = −16 V. The exponential behavior in the output curves is attributed to the Schottky barrier between the electrode and the polymer crystal. As a comparison, the reported photoconductive two-dimensional (2D) films of phosphine-thiolate-stabilized Au25 clusters [55], showed an ON/OFF ratio of about 50 000 for VSD = 6 V, charge carrier mobility approaching 10^{-5} cm^2 V^{-1} s^{-1} at VSD = 20 V, and n-type field effect. The mobility of the polymeric crystal $(AuAg)_{34n}$ is in the range of traditional *p*-type single-crystal organic semiconductors and close to the mobility of supercrystal of CdSe quantum dots [56–58]. The conductivity (1.49×10^{-5} S m^{-1}) of $(AuAu)_{34n}$ crystals in the *c*-crystallographic axis is one to three orders of magnitude higher than the values reported for thiolate-stabilized 1D assemblies of Au_{21} clusters where 1D "nanofibrils" of the clusters were formed by modulating the weak interactions between the ligand layers of the clusters [59]. These comparisons indicate that the conductivity and charge carrier mobility are increased by several orders of magnitude in the macroscopic cluster-based materials via direct linking of the clusters by the –Ag–Au–Ag– chains in the cluster polymer crystal.

1.4.3 Magnetism

$Au_{25}(SBu)_{18}^0$ is a paramagnetic monolayer-protected cluster that, in solution, displays the same molecule-like behavior of other Au_{25} clusters. In the solid state, however, a linear polymer $[Au_{25}(SBu)_{18}^0]_n$ composed of $Au_{25}(SBu)_{18}^0$ units interconnected by single Au—Au bonds is formed. The otherwise unpaired electrons of the $Au_{25}(SBu)_{18}^0$ clusters pair up, with the generation of a nonmagnetic ground state [46].

To explain this magnetic behavior, the authors conducted DFT calculations and compared the relative energies of the magnetic state and the nonmagnetic state of $[Au_{25}(SBu)_{18}^0]_n$. They found that in the crystal, the cluster has a nonmagnetic ground state that is lower in energy than the magnetic state by 27 meV. A nonmagnetic ground state implies that the otherwise unpaired electron in the isolated $Au_{25}(SBu)_{18}^0$ cluster is paired up in the ground state of the $Au_{25}(SBu)_{18}^0$ crystal, leading to a fully occupied valence band (VB) and an empty conduction band (CB). Further studies indicated that the energetics of nonmagnetic versus magnetic states are closely related to the intercluster distance or the closest Au–Au contact. When there is no close contact between two neighboring Au_{25} clusters, the magnetic state is preferred. On the other hand, when close contact occurs, the nonmagnetic state can be lower in energy than the magnetic state. The conclusion was supported by the reference research on two known clusters, $Au_{25}(SEt)_{18}^0$ and $Au_{25}(SC_2H_4Ph)_{18}^0$.

The authors also studied the cw-EPR behavior of the $[Au_{25}(SBu)_{18}^0]_n$ crystals in comparison with the spectrum obtained for a glassy toluene solution. The very different line width and the absence of a fine structure at 3000–4000 G for polymer $[Au_{25}(SBu)_{18}^0]_n$ show that the physical state in which $Au_{25}(SBu)_{18}^0$ is studied markedly affects the EPR signal. More specifically, the clusters in frozen solution display

the spectrum of distribution of randomly oriented $S = 1/2$ spin-state molecules with anisotropic g-tensor components. The temperature-dependent cw-EPR spectra of $[Au_{25}(SBu)_{18}^0]_n$ crystals and the estimated coupling energy (J) with the Hall expression revealed the fact that the double integrated EPR signal is an increasing function of T, indicating that thermal activation makes a higher energy magnetic state more populated, thereby confirming the DFT prediction that the ground state of $[Au_{25}(SBu)_{18}^0]_n$ is nonmagnetic. The best fit to the experimental data yields a J value of 28(2) meV, i.e. virtually identical to the DFT-calculated value of 27 meV. This outstanding agreement between EPR results and calculations thus provides compelling evidence that the $Au_{25}(SBu)_{18}^0$ clusters self-organize into a linear $S = 1/2$ antiferromagnetic polymer chain.

1.5 Conclusion

This chapter summarizes the surface engineering and hierarchical assembly of gold NCs with atom-precise composition and molecular structures. The surface modification of gold NCs is sorted out in detail according to different strategies, while the GCAMs are categorized by types of intercluster interactions. We gave an outline of the crystal structures of some typical examples and analyzed the opportunities and challenges. Benefiting from the novel structure features of the individual/aggregated metal cluster nodes, GCAMs show potential applications in many fields, including biomedicine, semiconductivity, and magnetism, to name a few. Several attractive representatives are introduced in the chapter.

In future work, new approaches to modify the ligand shell of gold NCs should be explored, which could conquer the shortcomings of gold NCs in specific applications. Controllable and designable GCAMs are desired in regard to the random assembly of hierarchical structures based on gold NCs. Also, the applications of gold-NC-based materials should be further pursued according to their functionality and advantages.

References

1 Chakraborty, I. and Pradeep, T. (2017). Atomically precise clusters of noble metals: emerging link between atoms and nanoparticles. *Chem. Rev.* 117: 8208–8271.
2 Jin, R., Zeng, C., Zhou, M., and Chen, Y. (2016). Atomically precise colloidal metal NCs and nanoparticles: fundamentals and opportunities. *Chem. Rev.* 116: 10346–10413.
3 Kang, X., Li, Y., Zhu, M., and Jin, R. (2020). Atomically precise alloy NCs: syntheses, structures, and properties. *Chem. Soc. Rev.* 49: 6443–6514.
4 Jin, Y., Zhang, C., Dong, X.-Y. et al. (2021). Shell engineering to achieve modification and assembly of atomically-precise silver clusters. *Chem. Soc. Rev.* 50: 2297–2319.

5 Chakraborty, P., Nag, A., Chakraborty, A., and Pradeep, T. (2019). Approaching materials with atomic precision using supramolecular cluster assemblies. *Acc. Chem. Res.* 52: 2–11.

6 Kang, X. and Zhu, M. (2019). Intra-cluster growth meets inter-cluster assembly: the molecular and supramolecular chemistry of atomically precise NCs. *Coordin. Chem. Rev.* 394: 1–38.

7 Zhang, M.-M., Li, K., and Zang, S.-Q. (2020). Progress in atomically precise coinage metal clusters with aggregation-induced emission and circularly polarized luminescence. *Adv. Opt. Mater.* 8: 1902152.

8 Goswami, N., Yao, Q., Luo, Z. et al. (2016). Luminescent metal NCs with aggregation-induced emission. *J. Phys. Chem. Lett.* 7: 962–975.

9 Rival, J.V., Mymoona, P., Lakshmi, K.M. et al. (2021). Self-assembly of precision noble metal NCs: hierarchical structural complexity, colloidal superstructures, and applications. *Small* 17: 2005718.

10 Luo, L. and Jin, R. (2021). Perspective atomically precise metal NCs meet metal-organic frameworks. *Iscience* 24: 103206.

11 Wang, Y. and Bürgi, T. (2021). Ligand exchange reactions on thiolate-protected gold NCs. *Nanoscale Adv.* 3: 2710–2727.

12 Dass, A., Stevenson, A., Dubay, G.R. et al. (2008). Nanoparticle MALDI-TOF mass spectrometry without fragmentation: $Au_{25}(SCH_2CH_2Ph)_{18}$ and mixed monolayer $Au_{25}(SCH_2CH_2Ph)_{18}$-x(L)x. *J. Am. Chem. Soc.* 130: 5940–5946.

13 Templeton, A.C., Wuelfing, W.P., and Murray, R.W. (2000). Monolayer protected cluster molecules. *Acc. Chem. Res.* 33: 27–36.

14 Guo, R., Song, Y., Wang, G.L., and Murray, R.W. (2005). Does core size matter in the kinetics of ligand exchanges of monolayer-protected au clusters? *J. Am. Chem. Soc.* 127: 2752–2757.

15 Shibu, E.S., Muhammed, M.A.H., Tsukuda, T., and Pradeep, T. (2008). Ligand exchange of $Au_{25}SG_{18}$ leading to functionalized gold clusters: spectroscopy, kinetics, and luminescence. *J. Phys. Chem. C* 112: 12168–12176.

16 Meng, X., Xu, Q., Wang, S., and Zhu, M. (2012). Ligand-exchange synthesis of selenophenolate-capped Au_{25} NCs. *Nanoscale* 4: 4161–4165.

17 Kurashige, W., Yamaguchi, M., Nobusada, K., and Negishi, Y. (2012). Ligand-induced stability of gold NCs: thiolate versus selenolate. *J. Phys. Chem. Lett.* 3: 2649–2652.

18 Zhong, J., Tang, X., Tang, J. et al. (2015). Density functional theory studies on structure, ligand exchange, and optical properties of ligand-protected gold NCs: thiolate versus selenolate. *J. Phys. Chem. C* 119: 9205–9214.

19 Niihori, Y., Matsuzaki, M., Pradeep, T., and Negishi, Y. (2013). Separation of precise compositions of noble metal clusters protected with mixed ligands. *J. Am. Chem. Soc.* 135: 4946–4949.

20 Heinecke, C.L., Ni, T.W., Malola, S. et al. (2012). Structural and theoretical basis for ligand exchange on thiolate monolayer protected gold NCs. *J. Am. Chem. Soc.* 134: 13316–13322.

21 Ni, T.W., Tofanelli, M.A., Phillips, B.D., and Ackerson, C.J. (2014). Structural basis for ligand exchange on $Au_{25}(SR)_{18}$. *Inorg. Chem.* 53: 6500–6502.

22 Yuan, X., Zhang, B., Luo, Z. et al. (2014). Balancing the rate of cluster growth and etching for GramScale synthesis of thiolate-protected Au_{25} NCs with atomic precision. *Angew. Chem. Int. Ed.* 53: 4623–4627.

23 Knoppe, S., Dharmaratne, A.C., Schreiner, E. et al. (2010). Ligand exchange reactions on Au_{38} and Au_{40} clusters: a combined circular dichroism and mass spectrometry study. *J. Am. Chem. Soc.* 132: 16783–16789.

24 Knoppe, S., Azoulay, R., Dass, A., and Bürgi, T. (2012). In situ reaction monitoring reveals a diastereoselective ligand exchange reaction between the intrinsically chiral $Au_{38}(SR)_{24}$ and chiral thiols. *J. Am. Chem. Soc.* 134: 20302–20305.

25 Wang, Y. and Bürgi, T. (2022). Evidence for stereoelectronic effects in ligand exchange reactions on Au_{25} NCs. *Nanoscale* 14: 2456–2464.

26 Suzuki, W., Takahata, R., Chiga, Y. et al. (2022). Control over ligand-exchange positions of thiolate-protected gold NCs using steric repulsion of protecting ligands. *J. Am. Chem. Soc.* 144: 12310–12320.

27 Lei, Z., Wan, X.-K., Yuan, S.-F. et al. (2018). Alkynyl approach toward the protection of metal NCs. *Acc. Chem. Res.* 51: 2465–2474.

28 Sugiuchi, M., Shichibu, Y., Nakanishi, T. et al. (2015). Cluster–π electronic interaction in a superatomic Au_{13} cluster bearing r-bonded acetylide ligands. *Chem. Commun.* 51: 13519–13522.

29 Hosier, C.A., Anderson, I.D., and Ackerson, C.J. (2020). Acetylide-for-thiolate and thiolate-for-acetylide exchange on gold NCs. *Nanoscale* 12: 6239–6242.

30 Narouz, M.R., Osten, K.M., Unsworth, P.J. et al. (2019). N-heterocyclic carbene-functionalized magic-number gold NCs. *Nat. Chem.* 11: 419–425.

31 Cao, Z., Gao, H., Qiu, M. et al. (2020). Chirality transfer from sub-nanometer biochemical molecules to sub-micrometer plasmonic metastructures: physiochemical mechanisms, biosensing, and bioimaging opportunities. *Adv. Mater.* 32: 1907151.

32 Yi, H., Osten, K.M., Levchenko, T.I. et al. (2021). Synthesis and enantioseparation of chiral Au_{13} nanoclusters protected by bis-N-heterocyclic carbene ligands. *Chem. Sci.* 12: 10436–10440.

33 Shen, H., Wu, Q., Malola, S. et al. (2022). N-heterocyclic carbene-stabilized gold nanoclusters with organometallic motifs for promoting catalysis. *J. Am. Chem. Soc.* 144: 10844–10853.

34 Luo, P., Bai, S., Wang, X. et al. (2021). Tuning the magic sizes and optical properties of atomically precise bidentate N-heterocyclic carbene-protected gold nanoclusters via subtle change of N-substituents. *Adv. Opt. Mater.* 9: 2001936.

35 Narouz, M.R., Takano, S., Lummis, P.A. et al. (2019). Robust, highly luminescent Au_{13} superatoms protected by N-heterocyclic carbenes. *J. Am. Chem. Soc.* 141: 14997–15002.

36 Kulkarni, V.K., Khiarak, B.N., Takano, S. et al. (2022). N-heterocyclic carbene-stabilized hydrido Au_{24} nanoclusters: synthesis, structure, and electrocatalytic reduction of CO_2. *J. Am. Chem. Soc.* 144: 9000–9006.

37 Lummis, P.A., Osten, K.M., Levchenko, T.I. et al. (2022). NHC-stabilized Au_{10} nanoclusters and their conversion to Au_{25} nanoclusters. *JACS Au* 2: 875–885.

38 Man, R.W.Y., Yi, H., Malola, S. et al. (2022). Synthesis and characterization of enantiopure chiral bis NHC-stabilized edge-shared Au10 nanocluster with unique prolate shape. *J. Am. Chem. Soc.* 144: 2056–2061.

39 Pei, X.-L., Zhao, P., Ube, H. et al. (2022). Asymmetric twisting of C-centered octahedral gold(I) clusters by chiral N-heterocyclic carbene ligation. *J. Am. Chem. Soc.* 144: 2156–2163.

40 Gabbaï, F.P., Schier, A., Riede, J., and Schmidbaur, H. (1997). Synthesis of the hexakis[(triphenylphosphane)gold(I)]methanium(2+) cation from trimethylsilyldiazomethane; crystal structure determination of the tetrafluoroborate salt. *Chem. Ber.* 130: 111–113.

41 Jia, J.-H. and Wang, Q.-M. (2009). Intensely luminescent gold(I)–silver(I) cluster with hypercoordinated carbon. *J. Am. Chem. Soc.* 131: 16634–16635.

42 Lei, Z., Pei, X.-L., Guan, Z.-J., and Wang, Q.-M. (2017). Full protection of intensely luminescent gold(I)–silver(I) cluster by phosphine ligands and inorganic anions. *Angew. Chem. Int. Ed.* 56: 7117–7120.

43 Gunawardene, P.N., Corrigan, J.F., and Workentin, M.S. (2019). Golden opportunity: a clickable azide-functionalized $[Au_{25}(SR)_{18}]-$ NC platform for interfacial surface modifications. *J. Am. Chem. Soc.* 141: 11781–11785.

44 Narita, K., Ishida, Y., Nukui, S. et al. (2021). Surface menshutkin S_N2 reaction on basic gold clusters provides novel opportunities for the cationization and functionalization of molecular metal clusters. *J. Phys. Chem. Lett.* 12: 11761–11765.

45 Saito, Y., Murata, C., Sugiuchi, M. et al. (2022). Ligand-coordinated metal clusters in condensed states: self-assemblies, crystals, and covalent networks. *Coordin. Chem. Rev.* 470: 214713.

46 De Nardi, M., Antonello, S., Jiang, D.E. et al. (2014). Gold nanowired: a linear $(Au_{25})_n$ polymer from Au_{25} molecular clusters. *ACS Nano* 8: 8505–8512.

47 Yuan, P., Zhang, R., Selenius, E. et al. (2020). Solvent-mediated assembly of atom-precise goldsilver NCs to semiconducting one-dimensional materials. *Nat. Commun.* 11: 2229.

48 Antonello, S., Dainese, T., Pan, F. et al. (2017). Electrocrystallization of monolayer-protected gold clusters: opening the door to quality, quantity, and new structures. *J. Am. Chem. Soc.* 139: 4168–4174.

49 Sokolowska, K., Hulkko, E., Lehtovaara, L., and Lahtinen, T. (2018). Dithiol-induced oligomerization of thiol-protected gold NCs. *J. Phys. Chem. C* 122: 12524–12533.

50 Jupally, V.R., Kota, R., Dornshuld, E.V. et al. (2011). Interstaple dithiol cross-linking in $Au_{25}(SR)_{18}$ nanomolecules: a combined mass spectrometric and computational study. *J. Am. Chem. Soc.* 133: 20258–20266.

51 Sels, A., Salassa, G., Cousin, F. et al. (2018). Covalently bonded multimers of $Au_{25}(SBut)_{18}$ as a conjugated system. *Nanoscale* 10: 12754–12762.

52 Lei, Z., Pei, X.-L., Jiang, Z.-G., and Wang, Q.-M. (2014). Cluster linker approach: preparation of a luminescent porous framework with NbO topology by linking silver ions with gold(I) clusters. *Angew. Chem. Int. Ed.* 53: 12771–12775.

53 Chang, H., Karan, N.S., Shin, K. et al. (2021). Highly fluorescent gold cluster assembly. *J. Am. Chem. Soc.* 143: 326–334.

54 Yan, L.-L., Yao, L.-Y., Ng, M., and Yam, V.W.-W. (2021). Stimuli-responsive and structure-adaptive three-dimensional gold(I) cluster cages constructed via "De-aurophilic" interaction strategy. *J. Am. Chem. Soc.* 143: 19008–19017.

55 Galchenko, M., Black, A., Heymann, L., and Klinke, C. (2019). Field effect and photoconduction in Au_{25} NCs films. *Adv. Mater.* 31: e1900684.

56 Jiang, H. and Hu, W. (2020). The emergence of organic single-crystal electronics. *Angew. Chem. Int. Ed.* 59: 1408–1428.

57 Chu, I.-H., Radulaski, M., Vukmirovic, N. et al. (2011). Charge transport in a quantum dot supercrystal. *J. Phys. Chem. C* 115: 21409–21415.

58 Talgorn, E., Abellon, R.D., Kooyman, P.J. et al. (2010). Supercrystals of CdSe quantum dots with high charge mobility and efficient electron transfer to TiO_2. *ACS Nano* 4: 1723–1731.

59 Li, Q., Russell, J.C., Luo, T.-Y. et al. (2018). Modulating the hierarchical fibrous assembly of au nanoparticles with atomic precision. *Nat. Commun.* 9: 3871.

60 Bonacchi, S., Antonello, S., Dainese, T., and Maran, F. (2021). Atomically precise metal NCs: novel building blocks for hierarchical structures. *Chem. Eur. J.* 27: 30–38.